

First results from the adaptive optics system from LCRD's Optical Ground Station One

**Lewis C. Roberts Jr., Gary L. Block, Santos F. Fregoso, Harrison Herzog, Seth R. Meeker,
Jennifer E. Roberts, Jonathan A. Tesch, Tuan N. Truong & Joshua D. Rodriguez**

*Jet Propulsion Laboratory, California Institute of Technology,
4800 Oak Grove Dr., Pasadena CA 91109, USA*

Andrew Bechter

*Department of Physics, University of Notre Dame,
225 Nieuwland Science Hall, Notre Dame, IN 46556, USA*

Abstract

The Laser Communication Relay Demonstration is NASA's multi-year demonstration of laser communication to a geosynchronous satellite. The mission currently has two optical ground stations (OGS), with one in California (OGS1) and one in Hawaii (OGS2). This summer we deployed the optical system for OGS1 to the 1-meter OCTL telescope in Wrightwood CA. The optical system consists of an high order adaptive optics system, the transmit system and a camera for target acquisition. The adaptive optics system is responsible for compensating the downlink beam for atmospheric turbulence and coupling it into the modem's single mode fiber. It is required to operate at 20 degrees above the horizon and produce Strehl ratios of greater than 70% in both daytime and nighttime. To meet this requirement, the adaptive optics system uses two deformable mirrors with one mirror correcting for low spatial frequencies aberrations with large amplitude and a second deformable mirror correcting for high spatial frequencies aberrations with small amplitude. The system uses a Shack-Hartmann wavefront sensor. The transmit system relays four beacon beams and one communication laser to the telescope for propagation to the space terminal. Both the uplink and downlink beams are centered at 1.55 microns. We present an overview of the design of the system, predicted performance predictions and measured system performance.

1. INTRODUCTION

The Laser Communications Relay Demonstration (LCRD) project is NASA's multi-year demonstration of laser communication between multiple ground stations and a geosynchronous satellite. LCRD will provide high data rate optical communications, demonstrating that optical communications can meet NASA's growing need for higher data rates while also enabling lower power, lower mass communications systems on spacecraft. In addition, LCRD's architecture will serve as a developmental test bed for additional methods, including symbol coding, ranging, link layer protocols, and network layer protocols[1]. LCRD will serve as a test bed for future NASA missions including the development of a future Advanced Telecommunications and Data Relay Satellite Service[2]. The mission is led by Goddard Space Flight Center (GSFC) with the participation of Massachusetts Institute of Technology-Lincoln Laboratory and Jet Propulsion Laboratory (JPL).

The LCRD space terminal will be a hosted payload on the U.S. Air Force's Space Test Program Satellite-6 (STPSat-6 [3] in geosynchronous orbit. The space terminal is capable of simultaneously communicating with two ground stations. There are currently two optical ground stations. Optical Ground station 1 (OGS1) is located at JPL's Table Mountain Observatory in Wrightwood California[4]. It will use the 1-m Optical Communication Telescope Laboratory (OCTL) telescope[5]. Optical Ground station 2 (OGS2) will be located at the U.S. Air Force's Maui Space Surveillance System on top of Haleakala in Maui, Hawaii. It will use a 0.6m receive telescope and a 0.15m transmit telescope [6].

Optical Ground station 1 (OGS1) consists of multiple systems including the existing OCTL telescope, the communication and beacon lasers, the monitor and control system, laser safety and the Integrated Optical System (IOS), which is the subject of this paper. The IOS system has two major functions. The first is to relay light from the beacon and communication lasers to the telescope. The second function is to relay the received light from the telescope to the ground modem's single mode fiber. Coupling the light into the single mode fiber requires an adaptive optics system that produces high Strehl ratios.

2. ADAPTIVE OPTICS SYSTEM

A number of requirements were levied on the IOS. Of those, three drive the complexity of the system. As the exact location of the host satellite was unknown at the start of the design process, the IOS is required to operate at elevation angles as low as 20° . Recently the satellite location was specified to be between $112\text{-}120^\circ$ with a target of 107° . This puts it at an elevation angle of 50° for OGS1. The system is also required to work at the median seeing conditions at Table Mountain, or a Fried's parameter of 5.2 cm measured at zenith at a wavelength of 500 nm. Finally the system was required to work day or night. Under these conditions the IOS is required to produce a coupling efficiency of 55%, which translates to a Strehl ratio of roughly 70%. The nominal received power levels will be 125nW/m^2 at the front of the IOS.

AO is a technique where a deformable mirror is used to correct aberrations in the wavefront. These aberrations are sensed by a wavefront sensor (WFS). There are multiple types of wavefront sensors, each with its own advantages and disadvantages. We chose a Shack-Hartmann sensor in a Fried geometry for the WFS. Most astronomical AO systems make their wavefront sensing measurements at one wavelength, and correct at another wavelength. For laser communication, where there is only a single incoming wavelength, we have to divert part of the incoming light to the WFS. The IOS has a baseline diversion of 20%, but we are reevaluating that based on the newly determined location of the satellite. The LCRD downlink wavelength is 1545 nm. The speed of the WFS measurement is critical for the AO system to keep up with the rapidly changing atmospheric turbulence conditions at the required 20° elevation and nominal r_0 of 5.2 cm. Our models have shown that we need to have frame rates on the order of 10 kHz to achieve our desired level of performance in the specified atmospheric conditions. The WFS camera is an off the shelf Xenics Cheetah InGaAs camera. Each lenslet in the WFS will illuminate an array of 2×2 detectors on the WFS focal plane array.

We carried out a trade study on the number of actuators across the primary. A higher actuator density will reduce the wavefront fitting error, but the WFS will have fewer photons per lenslet to make the wavefront measurements, which will increase the wavefront measurement error. In the end, we decided that 28 actuators across the primary mirror diameter would produce the best trade-off between fitting error and measurement error. This led us to the choice to use a Boston Micromachines 32×32 actuator Kilo-C MEMS DM[7] with a continuous facesheet. This DM only has an actuator stroke of $1.5\ \mu\text{m}$, which in turn drives us to use a woofer/tweeter design using the Boston Micromachines 12×12 actuator $3.5\ \mu\text{m}$ stroke Multi-DM in addition to the Kilo DM. Our current stroke budget shows that we need $3.1\ \mu\text{m}$ of stroke for the required 20° elevation angle, which gives us 12% margin. For the actual elevation angle of 50° , we will have 23% margin. In a woofer/tweeter design, a Low Order DM (LODM) corrects low spatial frequencies and large amplitude aberrations, while a High Order DM (HODM) corrects high spatial frequencies and small amplitude aberrations. MEMS DM have two advantages over conventional DMs. They are much smaller in diameter, on the order of 1 cm, which allows the rest of the optical train to be smaller. This reduces the cost of the optical train. Also the DMs themselves cost less than conventional DMs.

The IOS will be located in the coudé room of the OCTL facility. This room allows for multiple experiments to be set up simultaneously; a flat mirror on a rotation stage directs the optical beam to the desired experiment. The IOS will be located on a standard optical bench, and will be isolated from the room atmospheric turbulence with an enclosure that also blocks stray laser light from leaving the optical bench. The IOS components are mounted on four separate breadboards which are mounted on the optical bench, which is shown in Fig. 1 Having the IOS mounted on separate breadboards facilitates moving the system from the development laboratory to the telescope. Also, the WFS and a portion of the transmit system are aligned separately.

In the following description, we trace the light going through the receive system as it comes from the telescope. The description starts at the Transmit/Receive Dichroic. In Fig. 1, this is where the red line intersects the blue line. First the beam hits acquisition camera pickoff. A portion of the light gets diverted to a camera that images the uncompensated light. This is used to acquire the target and then to measure the Fried's parameter at 1 Hz. Next the light encounters the first of five off-axis parabola (OAP1) mirrors, which forms a pupil on the fast steering mirror (FSM). Then the downlink beam encounters OAP2 and OAP3, which form a second pupil on the HODM. The beam then encounters OAP4 and OAP5 which form a third pupil on the LODM. The next optic is a pair of filters that block any back scattering from the uplink beam from entering the downstream sensors. The wavefront sensor picks off 10% of the light with a beamsplitter. Another 10% of the light is picked off for the scoring camera. Then the

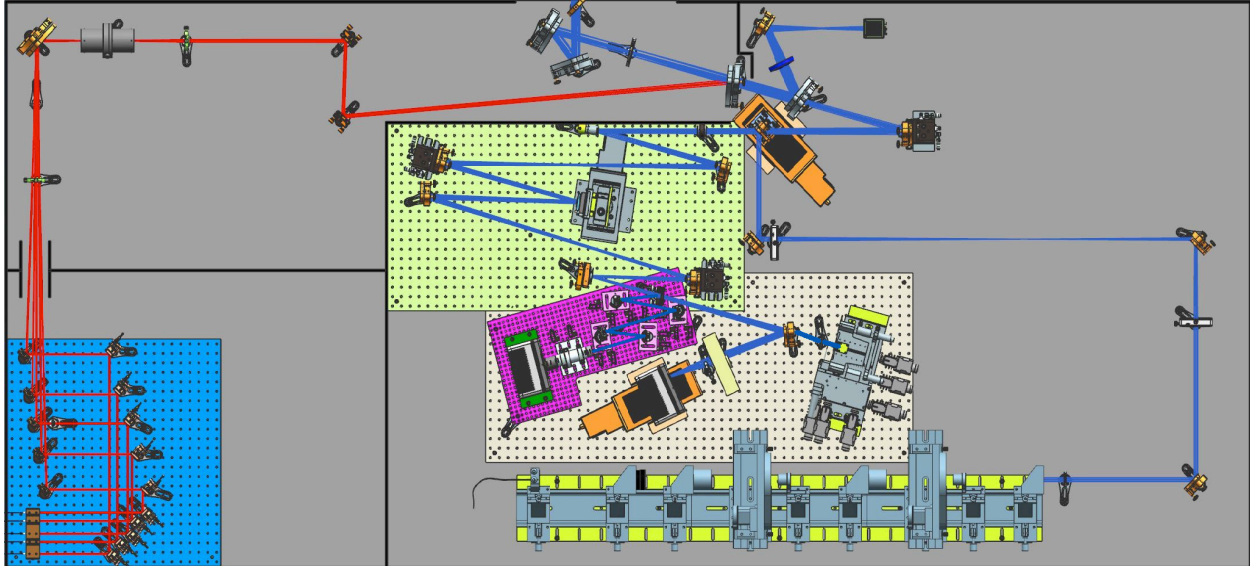


Fig. 1 The IOS opto-mechanical layout. The transmit arm is marked in red, and the AO arm in blue. The WFS is mounted on the purple breadboard. The remaining components in the AO arm are divided between the tan and green breadboards. Much of the transmit system is mounted on the blue bread board on the left. The Atmospheric Turbulence Simulator (ATS) is at the bottom of the layout.

light is coupled into the single mode fiber that goes to the ground terminal. The AO system takes up most of a fairly large optical bench. Long focal length OAPs were used to ease the alignment; for other applications the system could be made much more compact.

The system also has an atmospheric turbulence simulator (ATS). A mirror can be slid into the beam path to inject light from the ATS into the AO system. The beam has the same optical properties as the downlink from the telescope and forms pupil images at the same locations. The ATS consists of two spinning phase plates with computer controlled rotation rates to simulate a variety of turbulence conditions[8]. The ATS will allow the IOS AO system to be tested in the lab over a wide variety of atmospheric conditions. This will improve the quality of the AO system, so that it will be farther down the development path when it gets to the telescope. It can also be left on for several days to help find bugs that will impair operations. Doing this in the laboratory is much more efficient than doing it at the telescope saving time and labor costs. The telescope is a limited resource and can be closed due to inclement weather. Also, specific atmospheric conditions are not available on demand, but depend on the whim of nature. During operations the ATS will be used for regression testing when the system is started up. The performance on these standardized tests will allow us to track IOS performance over the course of the mission and hopefully detect failing components before they totally fail.

As mentioned above, a portion of the downlink beam is diverted to the scoring camera. The scoring camera produces an image of the compensated downlink beam. This is used to judge the quality of compensation by measuring the Strehl ratio. The IOS also receives a measurement of the received power in the modem, but that is slightly delayed and is also not available before the launch of the space terminal.

3. SOFTWARE ARCHITECTURE

The IOS software is based on the PALM-3000 software design[9]. Where functionally possible, existing PALM-3000 software was reused. We estimate that we have reused approximately 50% of the PALM-3000 code; this was a great time saver. As the IOS software is effectively a second generation version of the PALM-3000 code; this provides opportunities to incorporate lessons learned and to improve on the existing code.

The system design is divided into four main components: a command/automation server, a device driver server, the real-time control component, and the graphical user interface running on a computer in the operators room. The publish/subscribe communication method is used to transfer messages between components, a particularly effective

method for systems with components running in physically separate locations. The real-time component uses a Digital Signal Processor (DSP) board with eight on-board DSP chips. We use direct memory access (DMA) to get data from the frame grabber directly to the DSP board enabling us to achieve the required frame rates. All published data is written to the database in the form of commands, status messages, and telemetry data. A separate component acts as the interface to the database; a slightly enhanced version of the Berkeley DB database engine. A solid state drive in the IOS control computer is capable of capturing all of telemetry data types at the highest possible log rates. This will enable us to analyze performance during testing and operations.

Graphic Processor Units (GPU) based systems have become the standard for low latency AO real-time control systems [10, 11]. While GPU systems are able to meet latency requirements of many instruments in operation today, they are limited in their processing capability by two factors: the lack of GPU support for application-level direct access to PCI Express and the absence of frame grabbers with application-tuned direct memory access (DMA) transfer size capability. IOS has solved this problem by using a multi-DSP based real-time control system that leverages the PCI Express multicast capability and a DMA-tuned frame grabber. This is illustrated in Fig. 2.

As the WFS takes an image it is captured by the frame grabber. From the frame grabber, the image is read out row by row. When there are two rows of data available, it gets shipped to the DSP board. Each of the eight DSP chips on the board contains eight cores. Each of the 64 cores measures the centroids of all the lenslets, but each core is assigned specific DM Actuators to compute the commands for. When the commands are computed, the DMA controller on each DSP chip transfers the DM commands to the appropriate DM via DMA. All of the above steps are done via DMA, which bypasses the central processing unit (CPU) and eliminates the CPU timing jitter. This enables us to deliver processing rates in excess of 20 kHz and a latency in the single-digit microsecond range for 56x64 pixel frames.

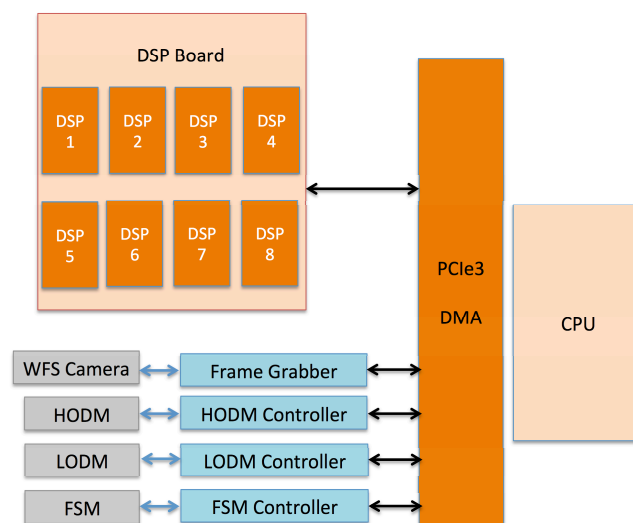


Fig. 2 Data are exchanged between the frame grabber, the DSP card and the active mirror elements via DMA, without going through the CPU, which would add timing jitter and increase the control loop latency, leading to degraded performance.

4. PERFORMANCE PREDICTIONS

We made performance predictions based on the AO error budget[12]. Strehl ratio, or image quality is the usual metric used to judge AO performance, but for optical communication what matters is how much light gets coupled into the detector, in our case a single mode fiber. The metric for that is coupling efficiency and defined as the fraction of the light immediately before the fiber that gets coupled into the fiber. In Fig. 3 we show the coupling efficiency as a function of Fried's parameter over the range of elevation angles that the space terminal could have been placed. As mentioned above, we recently have found out that it will be placed in the most optimal location. For

the required 20° elevation, the system would have met it's requirements of 55% coupling efficiency, but for the current 50°, we will have plenty of margin.

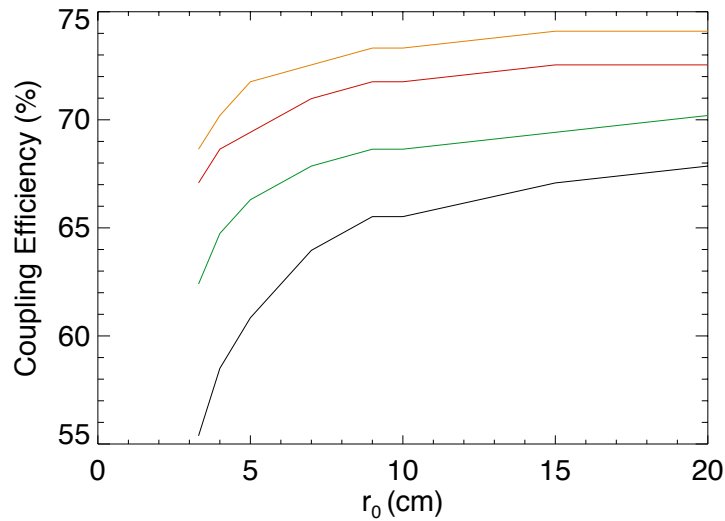


Fig. 3 The coupling efficiency as a function of turbulence conditions as measured by the Fried's parameter, r_0 . The different curves correspond to increasing elevation angle. The black curve is for 20°, the green curve is for 30°, the red curve is for 40° and the orange curve is for 50°.

While error budgets provide good insight into system performance, they assume constant properties of the atmosphere. To understand the temporal behavior of the system, we simulated time series of the coupling efficiency of the system using a wave optics simulation code based on FFT-based propagation and FFT-based phase screen generation. Five Kolmogorov turbulence layers were used for the simulations. Long simulation run times are enabled by slowly breaking the frozen flow hypothesis and adding a small component of a new Kolmogorov phase screen at each time step. The simulations were run for two cases both at an elevation angle of 20°. The first case was with nominal atmospheric conditions for Table Mountain of $r_0 = 5.2$ cm and a ground layer wind speed of 2.3 m/s. The second case was for conditions at 90% of the cumulative distribution function: $r_0 = 2.7$ cm and a ground layer wind speed of 5.3 m/s. In both cases, the wind profile used was the San Diego wind profile for the month of January [13]. This wind profile is the average of decades of twice daily radiosonde launches and was the nearest launch site to Table Mountain. The wind direction was set to be transversal to the line of sight. The simulation produced 10 runs with a duration of one second each for both conditions. The sampling rate was 10 kHz. The coupling efficiency time series is plotted in Fig. 4. The plot includes two consecutive 1 sec runs for the nominal conditions and for the 90th percentile case. At the higher wind speed and lower Fried parameter, the performance is more variable and produces a lower coupling efficiency. For the nominal case, the coupling efficiency is always above the required 0.55 value, while for the 90th percentile case, the average is just below the required level and sometimes much lower. This will result in degraded communication rates.

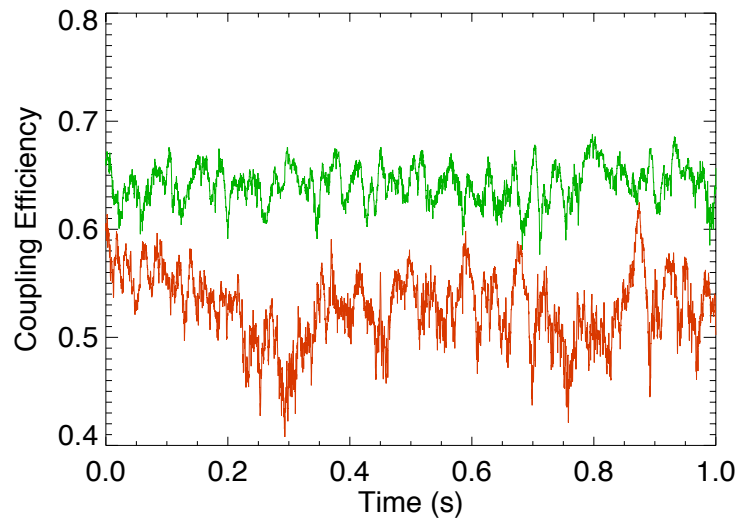


Fig. 4 The time series of coupling efficiency for an elevation of 20° . The green curve is the coupling for the nominal conditions, while the red curve is for the 90% conditions. The nominal conditions have an average value of 0.64 with a standard deviation of 0.0174, while the 90th percentile conditions have an average coupling of 0.53 with a standard deviation of 0.0331.

5. Features of the IOS

There are several aspects of the AO system that we think are interesting and somewhat unique. In this section, we briefly describe a few of these.

Modified Gerchberg-Saxton algorithm

Optical non-common path differences between the WFS and the science arm of the system can significantly degrade the performance of the AO system. To measure and correct those, we have implemented Modified Gerchberg-Saxton (MGS) algorithm[14]. This is a phase diversity algorithm which uses images measured at multiple defocus positions to compute the aberrated wavefront. The AO control loop is then instructed null this wavefront out. The technique has been used on many systems at JPL including testbeds and several adaptive optics systems [15].

In the IOS, the scoring camera is used to measure the non-common path aberrations in the system using the MGS algorithm. The scoring camera is located on a linear stage which provides the required focus diversity. The measured aberrations, which are not sensed by the WFS or only in the WFS arm, can then be corrected by the DMs leading to improved image quality. In Fig. 5 we show the a series of diversity images and the resulting reconstructed OPD.

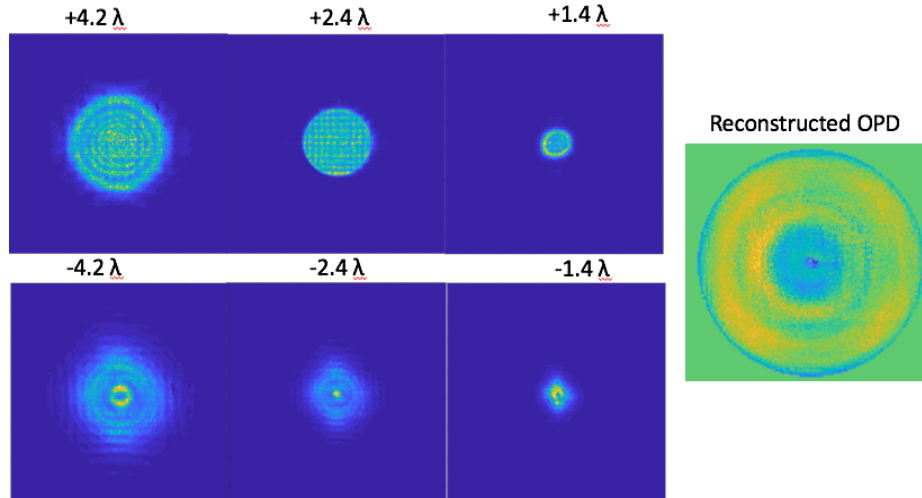


Fig. 5 The six figures on the left are PSF images taken at different foci. The image on the right is the reconstructed OPD using the MGS algorithm.

Measurement of Fried's Parameter

An understanding of Fried's parameter, r_0 , is useful for understanding the performance of an AO system. Differential image motion monitors (DIMM) are frequently used to measure site seeing, but they are almost always located at different locations than the AO system's telescope and are constrained to take measurements once every few minutes. When the seeing measurements are taken in a separate facility, it limits the ability to understand dome seeing. To mitigate these issues, we have developed a method for measuring r_0 from AO system's wavefront sensor using the slope discrepancy[16].

The slope discrepancy is the difference between the measured slopes and the slopes computed from a reconstructed wavefront reconstructed from the measured slopes[17]. The difference is caused by noise, turbulence and branch points. Branch points are not considered to be an issue for the IOS since we are observing in conditions with Rytov values less than 0.2. The noise is estimated from the measurements and this allows the technique to be used to measure the r_0 . The slope discrepancy is a useful measure because both result is the same if the AO system is operating open loop or closed loop.

Another benefit of the slope discrepancy is that a frame of WFS produces many measurements of the slope discrepancy which reduces the noise and increases the accuracy of the measurement. This allows a measurement of r_0 to be computed from only a few WFS frames increasing the measurement rate. This compares to other techniques that usually collect measurements every few minutes.

We developed this technique for the IOS, but deployed it to Palomar Observatory on the PALM-3000 AO system as a risk reduction effort. Fig. 6 shows an example. On 17 June 2016 UT, we collected data with the PALM-3000 AO system. The frame rate of the saved WFS data was 968 fps and we collected 9 seconds of data. For that night, we also had measurements for r_0 from the Palomar DIMM at a much lower frame rate. The r_0 values show general agreement. When the IOS is operational at the observatory, we plan to collect additional data and compare it with the DIMM at Table Mountain.

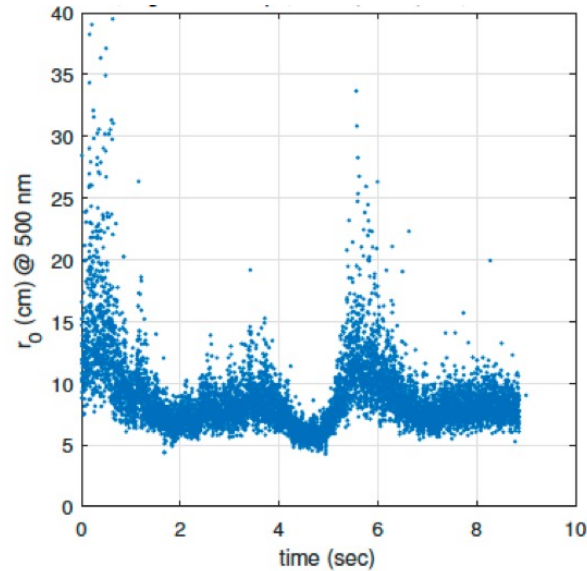


Fig. 6 A sample time series of r_0 taken at Palomar Observatory with the PALM-3000 AO system. Image credit T. Brennan.

Multi-channel Adaptive Control

Recent demonstrations have shown improved wavefront correction using optimal controllers, such as linear-quadratic regulators, which mitigate AO system latency and reduce broadband turbulence. These approaches typically include an offline procedure to identify models of the AO plant dynamics and external disturbances. However, high contrast imaging requires continuous closed-loop operation of many hours, and optical communication AO systems operate for long periods of time (for systems in geosynchronous orbit), or under rapidly changing conditions (for systems in low earth orbit). Both will benefit from a method for autonomously tracking non-stationary turbulence statistics.

Efforts are underway to implement a prototype adaptive control algorithm within the IOS real-time software architecture. The prototype is based on the receding horizon adaptive controller [18, 19] and uses a recursive least-squares lattice filter to implicitly track time-varying disturbance statistics. The controller is fully multichannel, providing joint adaptation over modes that may be spatially or temporally correlated.

Fig. 7 shows early simulation results comparing the performance of the receding horizon controller against a well-tuned integrator for a single spatial mode. The simulation was driven using open-loop disturbances collected from the IOS Atmospheric Turbulence Simulator, with the turbulence strength gradually increasing around $t=6.5$ sec. In this example the adaptive controller outperforms the integrator, and adapts to the new disturbance statistics when the turbulence strength is increased. The power spectrum of the adaptive control residuals are nearly white for the duration of the simulation, indicating that the controller fully exploits correlations in the disturbance statistics. We are currently implementing and testing multi-channel adaptive control on the IOS. With this control scheme, the AO system adapts to changing conditions and adjusts the loop behavior to maximize the system performance.

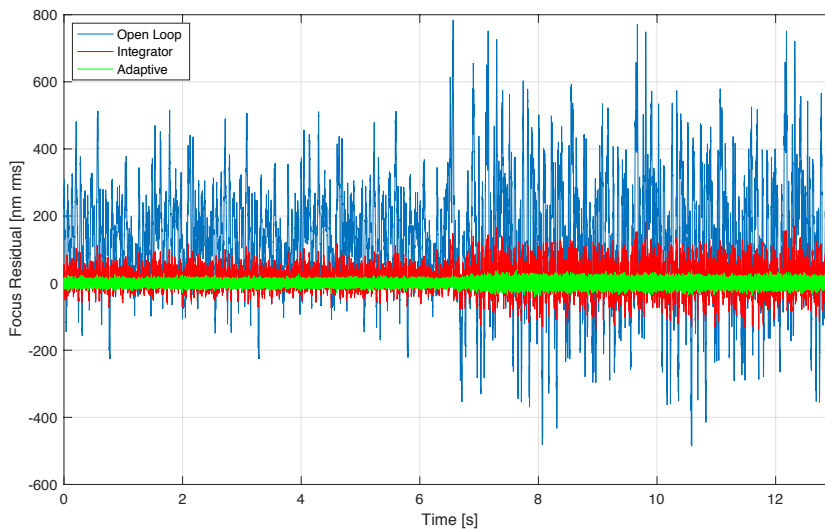


Fig. 7 Focus error residuals from a simulation comparing a classical integrator with a receding-horizon adaptive controller. The simulation used a turbulence sequence recorded from the IOS Atmospheric Turbulence Simulator

6. CONCLUSION AND FUTURE PLANS

When operational, the IOS system will be capable of achieving coupling efficiencies of greater than 50% in nominal atmospheric conditions at Table Mountain in California during daytime and nighttime. It will be a key enabling system for the LCRD project and will enable us to better understand how to build future ground stations.

The IOS has been fully integrated in the laboratory. We have closed the loop and are diagnosing the performance. One of the next steps we have to carry out is the removal of non-common path aberrations using the MGS algorithm. We will soon take it to the telescope. After realigning the system, we will begin a series of regression tests to confirm that the system is performing the same as it did in the laboratory. After that we will begin a series of on sky tests to further optimize the system. The LCRD mission's space terminal is scheduled to launch in October of 2019. The spacecraft will undergo system checkout when it reaches orbit; we expect to begin laser communication operations in early 2020.

The research was carried out at the Jet Propulsion Laboratory, California Institute of Technology, under a contract with the National Aeronautics and Space Administration (NASA).

7. REFERENCES

1. Luzhansky, E., et al. Overview and status of the Laser Communication Relay Demonstration, Proc. SPIE, Vol. 9739, 97390C-1, 2016.
2. Edwards, B.L, Israel, D., Wilson, K., Moores, J., and Fletcher, A., Overview of the Laser Communications Relay Demonstration project, Proc. of the International Conf. of Space Ops., 1261897, 2011.
3. Braun, B.M, Sims, S.M., McLeroy, J. and Brining, B., Breaking (space) barriers for 50 years: The past, present, and future of the DoD space test program, Proc. of the AIAA/USU Conf. on Small Satellites, SSC17-X-02, 2017.
4. Roberts, W.T. et al., Overview of Optical Ground Station 1 of the NASA Space Communications and Navigation Program, Proc. SPIE 9739, 97390B-1, 2016.
5. Wilson, K., Britcliffe, M. and Golshan, N. Progress in design and construction of the Optical Communications Telescope Laboratory (OCTL), Proc. SPIE, Vol. 3932, 112-116, 2000.
6. Edwards, B. L., Israel, D.J. and Vithlani, S.K., Latest changes to NASA's laser communications relay demonstration project, Proc. SPIE, Vol. 10524, 105240P, 2018.
7. Bifano, T., Shaping light: MOEMS deformable mirrors for microscopes and telescopes, Proc. SPIE, Vol. 7595, 759502, 2010.

8. Mantravadi, S., Rhoadarmer, T. and Glas, R., Simple laboratory system for generating well-controlled atmospheric-like turbulence, Proc. SPIE, Vol. 5553, 290–300, 2004.
9. Truong, T.N. et al., Design and implementation of the PALM-3000 real-time control system, Proc. SPIE, Vol. 8447, 844702F, 2012.
10. R. Dekany, et al., PALM-3000: Exoplanet adaptive optics for the 5 m Hale telescope, ApJ, Vol. 776, 130, 2013.
11. Sevin, A. et al., Enabling technologies for GPU driven adaptive optics real-time control, Proc. SPIE 9148, 91482G, 2014.
12. Hardy, J., *Adaptive Optics*, Oxford University Press, New York, NY, 1998.
13. Roberts, L. C. and Bradford, L. W., “Improved models of upper-level wind for several astronomical observatories,” Opt. Express, Vol. 19, 820–837, 2011.
14. Bikkannavar, S., et al. Phase Retrieval Methods for Wavefront Sensing, Proc. SPIE, Vol. 7739, 77392X, (1020)
15. Burruss, R. et al., Demonstration of on sky contrast improvement using the modified Gerchberg-Saxton algorithm at the Palomar Observatory, Proc. SPIE, Vol. 7736, 77365X, 2010.
16. Brennan, T. J. and Mann, D.C., Estimation of optical turbulence characteristics from Shack Hartmann wavefront sensor measurements, Proc. SPIE, Vol. 7816, 781602, 2010.
17. Tyler, G. A., Reconstruction and assessment of the least-squares and slope discrepancy components of the phase, J. Opt. Soc. Amer. A., Vol. 17, 1828–1839, 2000.
18. Tesch, J., Gibson, S., and Verhaegen, M., Receding-horizon adaptive control of aero-optical wavefronts, Opt. Eng, Vol. 52, 071406, 2013.
19. Tsuchiya, N., Gibson, S., Tsao, T.-C. and Verhaegen, M., Receding-horizon adaptive control of laser beam jitter, IEEE/ASME Trans. Mechatronics, Vol. 21, 227–237, 2015.